Numerical Study of Flow Characteristics due to Interaction Between a Pair of Vortices in a Turbulent Boundary Layer

Jang Sik Yang*
Advanced Environment & Energy Technology Research Institute,
K.K. Incinerator Engineering & Construction Co., Ltd.,
Inno-biz Center 206, Mandeok 3-dong, Buk-gu, Busan 616-829, Korea

This paper represents a numerical study of the flow field due to the interactions between a pair of vortices produced by vortex generators in a rectangular channel flow. In order to analyze longitudinal vortices induced by the vortex generators, the pseudo-compressibility method is introduced into the Reynolds-averaged Navier-Strokes equations of a 3-dimensional unsteady, incompressible viscous flow. A two-layer k-ε turbulence model is applied to a flat plate 3-dimensional turbulence boundary to predict the flow structure and turbulence characteristics of the vortices. The computational results predict accurately the vortex characteristics related to the flow field, the Reynolds shear stresses and turbulent kinetic energy. Also, in the prediction of skin friction characteristics the computational results are reasonably close to those of the experiment obtained from other researchers.

Key Words : Vortex Generator, Longitudinal Vortices, Pseudo-Compressibility, Half-delta Wing

1. Introduction

The vortices, which are produced by vortex generators, have an effect on flow and temperature fields because they have complicated three-dimensional turbulence characteristics. This flow, which has longitudinal velocity components, is an important phenomenon in fluid dynamics and heat transfer and it can disturb boundary layer structure strongly and affect heat transfer characteristics.

Many experimental studies on the heat transfer and the interactions between vortices in a turbulent boundary layer have been carried out. In addition, proper rules for the design and installation of vortex generators have been studied. Eibeck and Eaton (1987) have conducted experiments on longitudinal vortices embedded in a turbulent boundary layer and observed that the longitudinal vortices are found to influence heat transfer enhancement significantly. Pauley and Eaton (1988) studied two types of flow patterns induced by vortex generators with changing angles of attack; the flow between vortices is directed either away from the wall, common-flow-up, or toward the wall, common-flow-down. Numerical researchers have often used the experimental results of Pauley and Eaton to prove the validation of numerical schemes developed by them. The structure and development of streamwise vortex arrays embedded in a turbulent boundary were investigated by Wendt and Hingst (1994). Recently, studies on the performance of vortex generators, which are used as heat exchangers, have been performed widely.

With experimental studies, numerical studies focusing on the interactions between vortices and boundary layers have been carried out using the

* **E-mail** : yangjs@pusan.ac.kr
TEL : +82-51-336-6504; **FAX** : +82-51-336-6514
Advanced Environment & Energy Technology Research Institute, K.K. Incinerator Engineering & Construction Co., Ltd., Inno-biz Center 206, Mandeok 3-dong, Buk-gu, Busan 616-829, Korea. (Manuscript **Received** March 29, 2005; **Revised** November 16, 2005)

vortices generated by vortex generators as models. Using the PNS (Parabolarized Navier-Stokes) method, Anderson and Gibb (1992) performed a study on the longitudinal vortices induced by vortex generators. They also examined the fluid flow characteristics with respect to the geometric arrays of different vortex generators set up at the S-duct inlet. Numerical simulations of turbulent flows in a rectangular channel with mounted vortex generators on the bottom wall were carried out by Zhu et al. (1993). The flow field was computed by solving the Reynolds-averaged Navier-Stokes and energy equations, and the turbulence was taken into account by solving standard k-ε model equations with the wall law. Kim and Patel (1994) performed experimental and numerical studies of the interaction between the vortices and the turbulent boundary layer generated in the duct with flat plates and curvatures. Kim et al. (1996) studied heat transfer characteristics and flow structure in turbulent flows through a flat plate three-dimensional turbulent boundary layer containing built-in vortex generators using the PNS, the standard k-ε turbulent model and the eddy diffusivity. They concluded that heat transfer and skin friction showed relatively good results in comparison with experimental data and the heat transfer enhancement in the vicinity of the wall was due to the spanwise attachment of the vortices as they developed in the streamwise direction. Yang and Lee (2000) performed a numerical simulation of the common-flow-down induced by vortex generators. They observed that their results showed good agreement with the experiment of Pauley and Eaton (1988) and the computations of Kim et al.(1996). Lee and Kim (2004a and 2004b) studied the vortex flow characteristics of a sharp-edged delta wing at high angles of attack and concluded that an increase in the free stream velocity resulted in stronger leading edge vortices with an outboard movement and their computations provided qualitatively reasonable predictions of vertical flow characteristics, compared with past wind tunnel measurement.

As mentioned above, a better understanding of the heat transfer and flow field characteristics in a turbulent boundary layer with longitudinal vortices is very important in engineering designs, such as heat exchangers, mixing devices and controllers of separation flow. In the present study, the flow field behind vortex generators is modeled by the information obtained from studies on a delta wing. Three-dimensional Reynolds Navier-Stokes equations and a two-layer k-ε turbulent model are also used to analyze the vortices occurring behind the vortex generators. The numerical results obtained from the present study are compared with those of the experiment of Pauley and Eaton (1998).

2. Numerical Analysis

2.1 Governing equation

Three-dimensional unsteady, incompressible viscous flow can be defined as

Continuity equation

$$\frac{\partial u_i}{\partial x_i}=0 \tag{1}$$

Momentum equation

$$\frac{\partial \rho u_i}{\partial t}+\frac{\partial \rho u_i u_j}{\partial x_i}=-\frac{\partial p}{\partial x_i}+\frac{\partial \tau_{ij}}{\partial x_j} \tag{2}$$

Incompressible Navier-Stokes equations have the characteristics of an elliptic partial differential equation. However, if a pseudo-compressibility method is applied to solve the incompressible N-S equations, the system of equations given above can be solved efficiently because they can be given to a hyperbolic governing equation. This is similar to the case in which the steady, incompressible N-S equation is used for the compressible flow (Kwak et al., 1986).

Although the coordinate system in the present study is expressed in the cartesian coordinate system, the governing Eqs. (1) and (2) are defined in the generalized coordinate system to apply to complex geometries. The governing Eqs. (1) and (2), which employ the Boussinesq assumption and pseudo-compressibility, are made dimensionless and then transformed into the generalized coordinate system as follows:

$$\frac{\partial \hat{D}}{\partial \tau}=-\frac{\partial}{\partial \xi_i}(\hat{E}_i-\hat{E}_{vi}) \tag{3}$$

$$\hat{D}=\frac{D}{J}=\frac{1}{J}\begin{bmatrix} p \\ u \\ v \\ w \end{bmatrix} \tag{4}$$

$$\hat{E}_i=\frac{1}{J}\begin{bmatrix} \beta(U_i) \\ (\xi_i)_x p+u(U_i+(\xi_i)_\tau) \\ (\xi_i)_y p+v(U_i+(\xi_i)_\tau) \\ (\xi_i)_z p+w(U_i+(\xi_i)_\tau) \end{bmatrix} \tag{5}$$

$$\hat{E}_{vi}=\frac{1}{Re\cdot J}\begin{bmatrix} 0 \\ \nabla\xi_i\cdot\left(\nabla\xi_i\dfrac{\partial u}{\partial \xi_j}\right) \\ \nabla\xi_i\cdot\left(\nabla\xi_i\dfrac{\partial v}{\partial \xi_j}\right) \\ \nabla\xi_i\cdot\left(\nabla\xi_i\dfrac{\partial w}{\partial \xi_j}\right) \end{bmatrix} \tag{6}$$

where β and J are pseudo-compressibility parameter and Jacobian of the transformation, respectively, U_i means covariant velocity $(\xi_i)_x u+(\xi_i)_y v+(\xi_i)_z W$ and ξ_i indicates ξ, η and ζ for $i=1, 2, 3$.

2.2 Numerical methodology

The Crank-Nicolson method is used to obtain the secondary accuracy for time as follows:

$$\hat{D}^{n+1}=\hat{D}^n+\frac{\nabla\tau}{2}\left(\frac{\partial \hat{D}^n}{\partial \tau}+\frac{\partial \hat{D}^{n+1}}{\partial \tau}\right)+O(\Delta\tau^3) \tag{1}$$

The above equation can be linearized and summarized as

$$\left\{[I]+\frac{\Delta\tau}{2}J\delta_{\hat{\xi}_i}(\hat{A}_i^n-\Gamma_i)\right\}(D^{n+1}-D^n) =-\Delta\tau J\delta_{\hat{\xi}_i}(\hat{E}_i-\hat{E}_{vi})^n \tag{8}$$

Where,

$$\hat{A}_i=\frac{1}{J}\begin{bmatrix} 0 & (\xi_i)_x\beta & (\xi_i)_y\beta & (\xi_i)_z\beta \\ (\xi_i)_x & (\xi_i)_x u+U_i & (\xi_i)_y u & (\xi_i)_z u \\ (\xi_i)_y & (\xi_i)_x v & (\xi_i)_y v+U_i & (\xi_i)_z v \\ (\xi_i)_z & (\xi_i)_x w & (\xi_i)_y w & (\xi_i)_z w+U_i \end{bmatrix}$$

$$\Gamma_i=\frac{1}{\mathrm{Re}\cdot J}\left(\nabla\xi_i\cdot\nabla\xi_j I_m\frac{\partial}{\partial \xi_j}\right)$$

$$\delta_{\hat{\xi}_i}=\frac{\partial}{\partial \xi_i},\ I_m=diag[0,\ 1,\ 1,\ 1]$$

Then, after applying the AF algorithm, Eq. (8) is summarized and interpreted as

$$\begin{aligned}&\left\{[I]+\frac{\Delta\tau}{2}J\delta_{\hat{\xi}}(\hat{A}_1^n-\Gamma_1^n)\right\}\\ &\left\{[I]+\frac{\Delta\tau}{2}J\delta_{\eta}(\hat{A}_2^n-\Gamma_2^n)\right\}\\ &\left\{[I]+\frac{\Delta\tau}{2}J\delta_{\zeta}(\hat{A}_3^n-\Gamma_3^n)\right\}(D^{n+1}-D^n)\\ &=-\Delta\tau J[\delta_{\hat{\xi}}(\hat{E}_1-\hat{E}_{v_1})^n+\delta_{\eta}(\hat{E}_2-\hat{E}_{v_2})^n+\delta_{\zeta}(\hat{E}_3-\hat{E}_{v_3})^n]\end{aligned} \tag{9}$$

To ensure the stability of the numerical algorithm, a fourth-order artificial viscous term is applied in the residual terms, and the secondary or fourth-order artificial viscous term is applied in the implicit smoothing (Chang et al., 1988). Finally, the solutions to Eq. (9) can be obtained by applying the ADI algorithm.

2.3 Turbulence model

A two-layer turbulence model consisting of an inner layer and an outer layer is adopted: A one-equation model is used for the inner layer, and the standard $k-\varepsilon$ model is used for the outer layer. The one-equation model used for the inner layer needs only the solution of turbulent kinetic energy. In the inner layer, the eddy viscosity ν_t is equal to $C_\mu\sqrt{k}\,l_\mu$, and the dissipation ratio of turbulent kinetic energy ε is equal to $k^{\frac{2}{3}}/l_\varepsilon$. As shown below, the length scales, l_ε and l_μ, are used to give a damping effect necessary in the near-wall according to the turbulence Reynolds number $\left(R_y=\sqrt{k}\,\dfrac{y}{\nu}\right)$.

$$l_\mu=C_l y\left[1-\exp\left(-\frac{R_y}{70}\right)\right] \tag{10}$$

$$l_\varepsilon=C_l y\left[1-\exp\left(-\frac{R_y}{2C_l}\right)\right] \tag{11}$$

The constant C_l is given as $\kappa C_\mu^{-3/4}$ for a smooth-eddy viscosity distribution at the intersection of the inner layer and the outer layer, where κ is the von Karman constant. This two-layer model can be used in flow separation because the characteristic velocity near the wall is provided by turbulent kinetic energy rather than wall shear stress. Also, it does not require any boundary conditions for the calculation of the dissipation ratio.

2.4 Initial and boundary conditions

According to Phillips and Graham (1984), the velocity in the streamwise direction behind the vortex generator represents a Gaussian distribution, and the velocity in the circumferential direction appears as a Rankine vortex and the image of the Rankine vortex. Under these assumptions, the flow field in the streamwise direction and the velocity field in the circumferential direction are respectively defined as

$$U(r)=1-(\Delta U)_{\max}\exp\left\{-In\,2\left(\frac{r}{r_c}\right)^2\right\} \quad (12)$$

$$V_\theta=\begin{cases}(V_\theta)_c\dfrac{r}{r_c} & \text{for } r<r_c\\ (V_\theta)_c\dfrac{r_c}{r} & \text{for } r>r_c\end{cases} \quad (13)$$

Where $(\Delta U)_{\max}$ is the maximum axial velocity defect, $(V_\theta)_c$ is the maximum circumferential velocity, r_c is the half-radius of the vortex and C is the chord length of the vortex generator, i.e., $(\Delta U)_{\max}=1.0$, $(V_\theta)_c=0.501U_e$ and $r_c=0.018C$.

When the vortices with the above velocity distribution are introduced into boundary layers, there arises a transverse velocity component parallel to the wall, and the component is not zero at the wall. Therefore, the inner leg of Johnston's triangular plot for calculating cross flow in three-dimensional boundary layers is used to represent the cross directional velocity component (Johnston, 1960). Similar to the velocity in the streamwise direction, the turbulent kinetic energy and the eddy viscosity are respectively assumed to be a Gaussian distribution as shown below (Kim and Patel, 1994).

$$k(r)=k_{\max}\exp\left\{-In\,2\left(\frac{r}{r_c}\right)^2\right\} \quad (14)$$

$$\nu_t(r)=\nu_{\max}\exp\left\{-In\,2\left(\frac{r}{r_c}\right)^2\right\} \quad (15)$$

where $k_{\max}$ and $\nu_{\max}$ are given as $0.005U_\infty^2$ and 100ν, respectively.

The position of the vortex core is determined by referring to the α/β ratio of the delta-wing vortex generator and to a study of Lowson (1989), which examined the position and form of the vortices by visualizing them. The Y and Z positions of the vortex center are $0.24C$ and $0.48C$ in the case of common-flow-down and $0.24C$ and $0.32C$ in the case of common-flow-up, respectively. The half-delta wing vortex generators and the installed shape of them used in the experiment of Pauley and Eaton (1988) are shown in Fig. 1. The vortex generators have a chord length (C) of 5 cm, semi-span (b) of 2 cm at an angle of attack (α) of 18°. The Reynolds number based on the chord length of the half-delta wing is 55000. The working fluid is air and the freestream velocity is $U_e=16$ m/s. Fig. 2(a) shows the physical region. Fig. 2(b) illustrates the computation domain and the boundary conditions. For the computations of the flow field, the symmetric conditions are used for the left, right, and top faces, and the Neuman conditions for the downstream region. The inlet conditions use Eqs. (12)~(15). The no-slip conditions are used in the wall, and the turbulent kinetic energy in the wall (k_w) is zero.

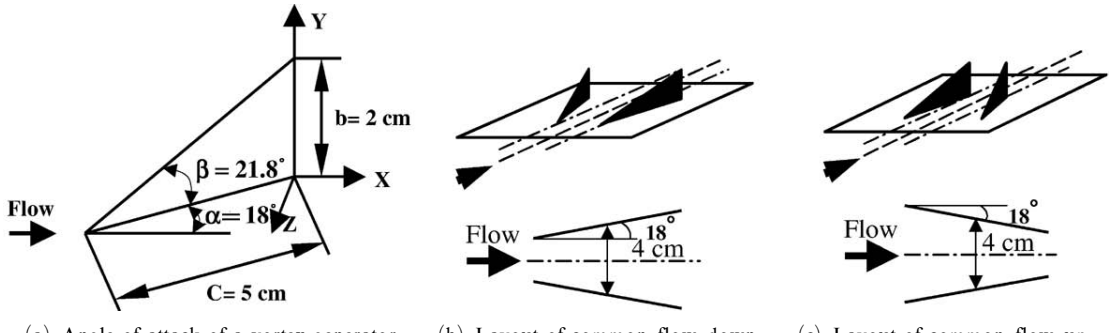

(a) Angle of attack of a vortex generator (b) Layout of common-flow-down (c) Layout of common-flow-up

Fig. 1 Schematic of vortex generators

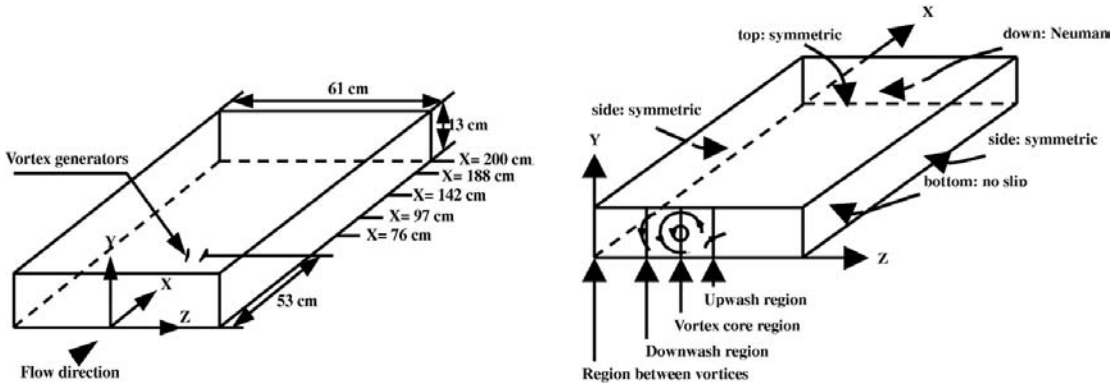

(a) Physical domain (b) Computation domain and boundary conditions

Fig. 2 Solution domain and boundary conditions

For X, Y, and Z, the computational grid point is selected as $47\times65\times57$ in the case of common-flow-down and $47\times80\times57$ in the case of common-flow-up, respectively.

3. Results and Discussion

3.1 Common-Flow-Down

Contours of the secondary velocity vector and streamwise velocity obtained from the computations are compared with those from the experiment of Pauley and Eaton (1988) at four axial locations in Figs. 3 and 4. It is clear that the general features of the experimental data are reproduced in the present results, although the velocity deficit at the vortex core is not resolved very well.

Fig. 3 shows the secondary velocity vectors at four planes downstream of the vortex generator (X=66, 97, 142 and 188 cm). As can be seen in Fig. 3, the secondary velocity vectors obtained from the computations represents generally well those from the experiment. The downwash flow toward the wall is observed between vortices, and the upwash flow away from the wall is found in the outside region of the vortices. As the vortices develop downstream, the magnitude of their velocity vectors decreases and the interval between them increases. This results in conservation of angular momentum and turbulence diffusion. The shape of the vortices reveals an ellipse expanded in the spanwise direction (Z direction). This is because the turbulence diffusion proceeds more rapidly in the numerical analysis than in the experimental data.

It can be seen from Fig. 4 that in the streamwise

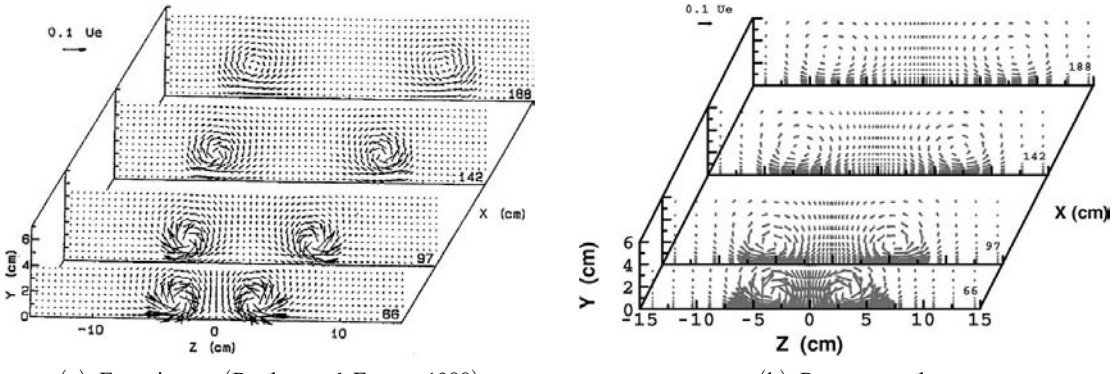

(a) Experiment (Pauley and Eaton, 1988) (b) Present result

Fig. 3 Secondary velocity vectors for common-flow-down at X=66, 97, 142, 188 cm

velocity contours the interaction of vortices has an immense influence on the change of the boundary layer thickness. The vortices impose a significant lateral divergence $(\partial W/\partial Z)$ in the central region. As a consequence, the boundary layer in the downwash region between the vortices is thinned quite, while the boundary layer is thickened markedly in the upwash region where the vortex sweeps low momentum fluid away from the wall. As the secondary velocities decay and the vortices spread apart, the lateral divergence decreases and the boundary layer grows. The streamwise velocity contours indicate a significant streamwise velocity deficit in the central region of the vortex. The velocity deficit decreases as the flow develops downstream.

Fig. 5 indicates that turbulent kinetic energy obtained from the present results is compared with that from the experiment at $X=97$ cm. The high level of turbulent kinetic energy can be observed near the wall. This energy is diffused by the primary vortex from the wall to the outer flow region. In addition, the strong turbulent energy is formed in the center of the vortex core while the weak turbulent energy is formed away from the wall to the upwash region. The predicted turbulent energy within the vortex core is lower than that obtained from the experiment. This difference can occur because there are not sufficient grid points in the vortex core to capture the rapid changes occurring there. Another reason is that the standard $k-\varepsilon$ model is intrinsically based on the isotropic concept. However, the predicted turbulent energy shows good agreement with that of the experimental data in the region of the near-wall and far away from the wall.

Fig. 6 represents the Reynolds stress $-\overline{uv}$ in the Z direction at $X=97$ cm. The high Reynolds shear stress appears at the top of the vortex, and a region of the Reynolds shear stress with a negative sign appears across the vortex core. A large region of negative shear stress is associated with the region of reversed velocity gradient. The present results represent the trends similar to

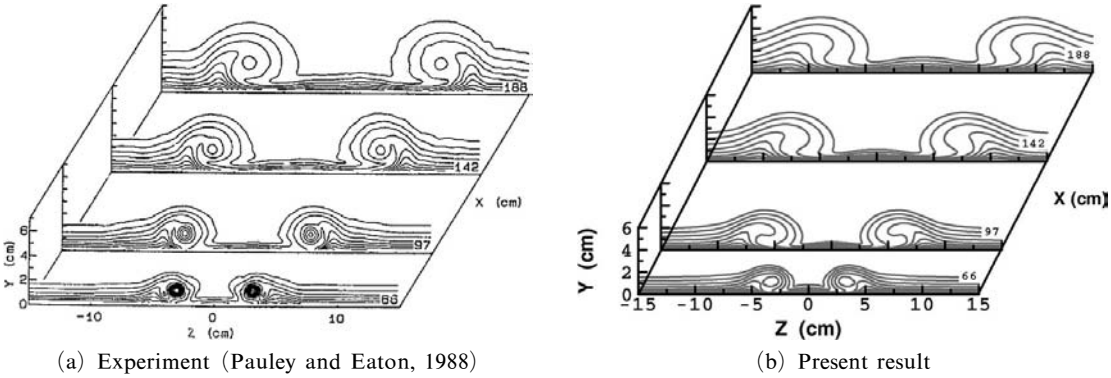

(a) Experiment (Pauley and Eaton, 1988) (b) Present result

Fig. 4 Streamwise velocity contours for common-flow-down at $X=66$, 97, 142, 188 cm

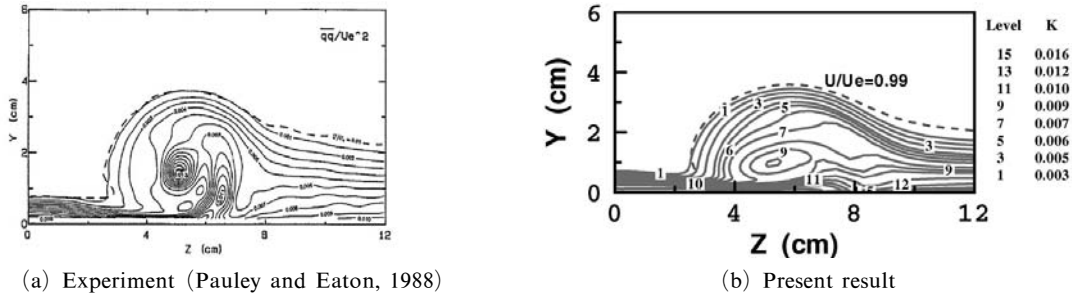

(a) Experiment (Pauley and Eaton, 1988) (b) Present result

Fig. 5 Turbulent kinetic energy for common-flow-down at $X=97$ cm

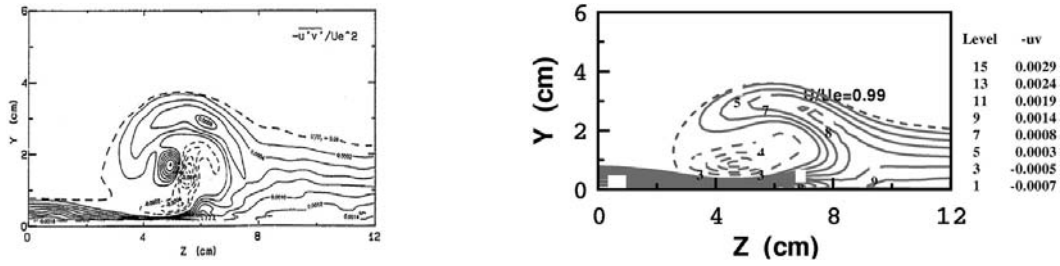

(a) Experiment (Pauley and Eaton, 1988) (b) Present result

Fig. 6 Reynolds shear stress for common-flow-down at $X=97$ cm

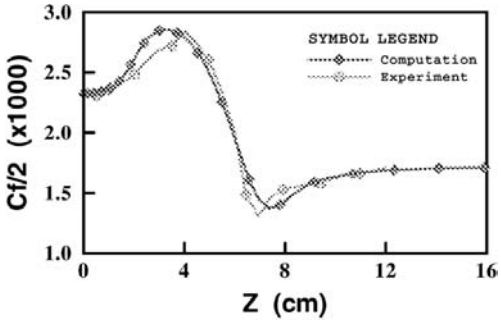

Fig. 7 Comparison of spanmwise components of skin friction for common-flow-down at $X=$ 97 cm

those observed in the experimental results of Pauley and Eaton (1988) except the region of the vortex core. Therefore, these similar trends give support to the two-layer $k-\varepsilon$ model insofar as longitudinal vortices are concerned.

As can be seen in Fig. 7, there is good agreement between the computations and the experimental data for the spawise distribution of the streamwise friction coefficients. The region between the vortices thins the boundary layer and leads to higher friction coefficient there. The upwash region where the low momentum fluid is lifted by the vortex shows lower fiction coefficient. The maximum value of the friction coefficient obtained from the computations is predicted higher than that from the experiment by about 4%. The minimum value of the friction coefficient obtained from the computations is predicted lower than that from the experiment by about 1%.

3.2 Common-Flow-Up

Contours of the secondary velocity vector and streamwise velocity obtained from the computation are compared with the experimental data of Pauley and Eaton (1988) at three axial locations ($X=66$, 97 and 142 cm) in Figs. 8 and 9. It is clear that the general features of the present results are reproduced well in the experimental data. Fig. 8 illustrates the secondary velocity vector in the streamwise direction of common-flow-up. The upwash flow occurs in the central region ($Z=0$ cm), and the downwash flow occurs outside the center. As the vortices move in the downstream region, the magnitude of the velocity vectors decreases. However, unlike common-flow-down, the distance between the vortices does not change and the lifting of the vortices from the wall increases conspicuously as the flow progresses downstream. This lifting of the vortices is due to the influences of the image vortices existing below the solid wall. These image vortices tend to move the vortices located at the upper part of the wall to the central region ($Z=0$ cm). As the vortices move downstream, they are convected from the wall by the strong interaction between the vortices that move to the central region. As a result, the vortices move up from the wall. As in common-flow-down, the shape of vortices becomes an ellipse in the vertical direction (Y direction).

Fig. 9 shows the streamwise velocity contours. The outer region of the constant velocity distribution in the streamwise direction means the free-stream velocity. As the spanwise velocity gradient ($\partial V/\partial Y$) in the Y direction increases, the boundary layer is thickened in the upwash region and thinned in the downwash region. This phenomenon occurs when the primary vortex

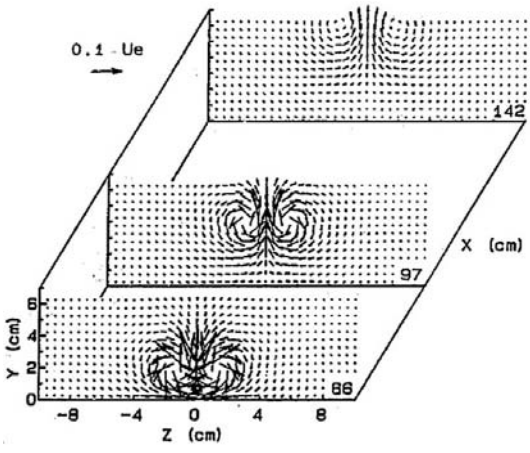

(a) Experiment (Pauley and Eaton, 1988)

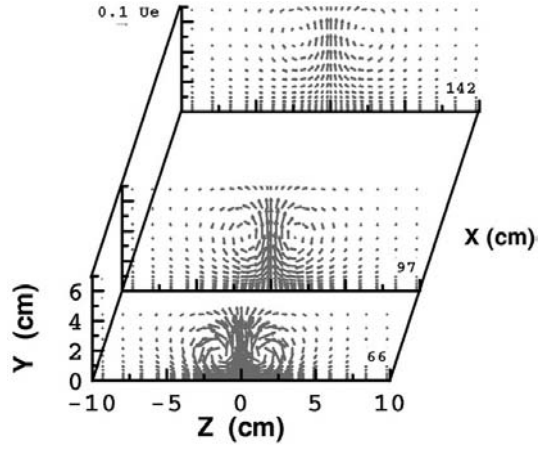

(b) Present result

Fig. 8 Secondary velocity vectors for common-flow-up at $X=66$, 97, 142 cm

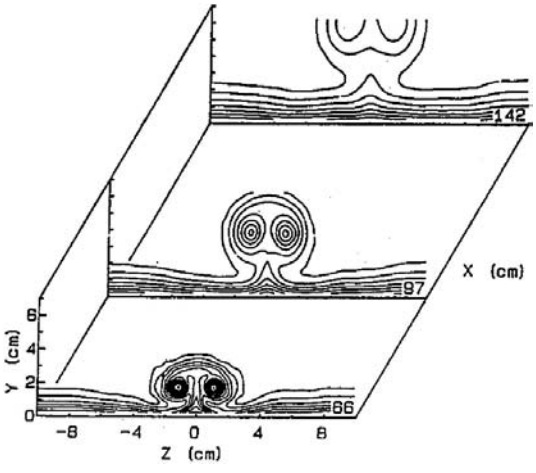

(a) Experiment (Pauley and Eaton, 1988)

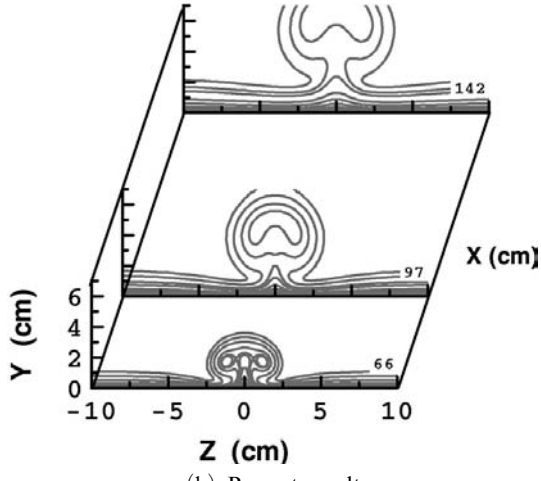

(b) Present result

Fig. 9 Streamwise velocity contours for common-flow-up at $X=66$, 97, 142 cm

moves low momentum fluid from the downwash region to the upwash region. Serious distortion of the boundary layer is observed in the region between the vortices. This phenomenon intensifies as the vortices move further downstream.

Fig. 10 represents turbulent kinetic energy at $X=97$ cm. The present results of turbulent kinetic energy show the trends similar to those observed in the experiment. The high level of turbulent kinetic energy appears near the wall. This energy is diffused by the primary vortex from the wall toward the outer flow. As in the case of common-flow-down, the strong turbulent energy forms in the center of the vortex, and the weak turbulent energy forms away from the wall to the upwash region. Although the predicted value in the vortex core is predicted lower than the experimental value, the overall trends are found to be reasonably similar to those obtained from the experimental results of Pauley and Eaton.

The distribution of the Reynolds shear stress $-\overline{uv}$ in the Z direction at $X=97$ cm is shown in Fig. 11. As can be seen in Fig. 11, unlike common-flow-down, the distribution of this stress is considerably distorted by the strong interactions between the vortices. There is a region of the high

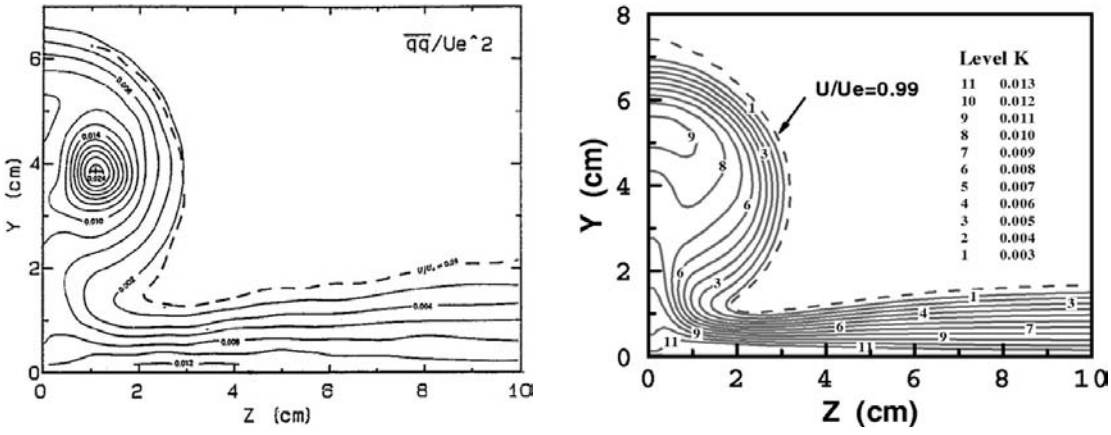

(a) Experiment (Pauley and Eaton, 1988) (b) Present result

Fig. 10 Turbulent kinetic energy for common-flow-up at $X=97$ cm

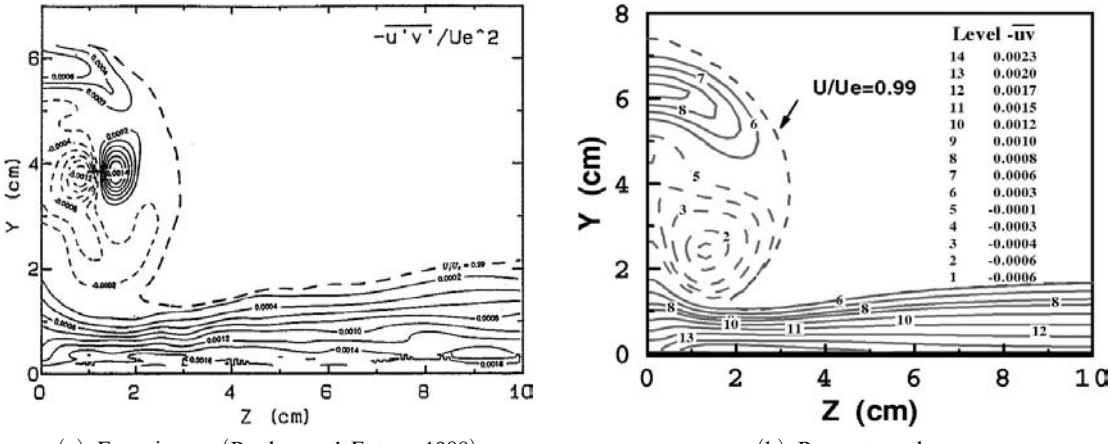

(a) Experiment (Pauley and Eaton, 1988) (b) Present result

Fig. 11 Reynolds shear stress for common-flow-up at $X=97$ cm

shear stress extending up through the upwash and a large region of the negative shear stress which is associated with the region of reversed velocity gradient. The computational results at all positions except the vortex core show very good agreement with those of the experimental data.

The profile of the streamwise friction coefficients along the spanwise direction at $X=97$ cm is shown in Fig. 12. Unlike common-flow-down, the effect of the vortices is seen only near the center zone ($Z=0$ cm). The change in the stremwise friction coefficient is smaller than that in common-flow-down since the common-flow-up disturbs the boundary layer much less than the common-flow-up. The maximum value of the

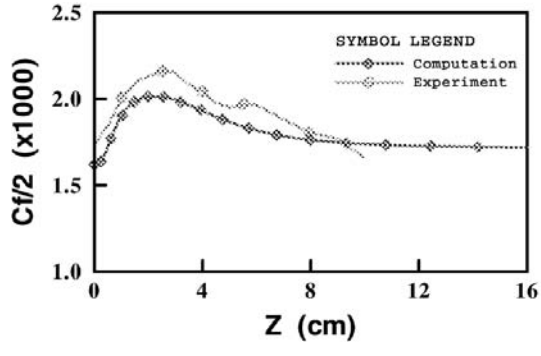

Fig. 12 Comparison of spanwise components of skin friction for common-flow-up at $X=97$ cm

friction coefficient obtained from the computation is predicted lower than that from the experi-

ment by about 7%.

4. Conclusions

In order to analyze the flow field induced by the vortex generators, the Reynolds-averaged Naiver Stokes equations for three-dimensional turbulent flows, together with a two-layer turbulence model to solve the near-wall flow, are solve by the AF-ADI algorithm. The following conclusions are made from numerical analysis. The boundary layer is thinned in the region where the secondary flow is directed toward the wall and thickened where it is directed away from the wall. In the case of common-flow-down, the interaction between the vortices becomes very weak but the interaction between the vortices and the boundary layer becomes very strong. On the other hand, in the case of common-flow-up, the interaction between the vortices becomes very strong but the interaction between the vortices and the boundary layer becomes very weak. In all the cases of both common-flow-down and common-flow-up, the strong turbulent energy is formed in the center of the vortex core while the weak turbulent energy is formed away from the wall to the upwash region. Also, the high Reynolds shear stress appears at the top of the vortex and a region of the Reynolds stress with a negative sign appears across the vortex core. In comparison with the experiment of Pauley and Eaton (1988), although some discrepancies are observed near the center of the vortex core, the overall performance of the present numerical analysis is found to be satisfactory. Therefore, the numerical scheme suggested may be used as a useful method for studies on the vortices in three-dimensional turbulent flows.

References

Anderson, B. H. and Gibb, J., 1992, "Application of Computational Fluid Dynamics to the Study of Vortex Flow Control for the Management of Inlet Distortion," *AIAA* paper 92-3177.

Chang, J. L. C., Kwak, D. C., Rogers, S. E. and Yang, R. J., 1988, "Numerical Simulation Methods of Incompressible Flows and an Application to the Space Shuttle Main Engine," *International Journal for numerical methods in fluids*, Vol. 8, pp. 1241～1268.

Eibeck, P. A. and Eaton, J. K., 1987, "Heat Transfer Effects of a Longitudinal Vortex Embedded in a Turbulent Boundary Layer," *Journal of Heat Transfer*, Vol. 109, pp. 16～24.

Johnston, J. P., 1960, "On the Three-Dimensional Turbulent Boundary Layer Generated by Secondary Flow," *Journal of Basic Engineering*, pp. 233～248.

Kim, J. Q., Ryou, H. S., Jeong, J. Y. and Dedousis, V., 1996, "Numerical Simulation of 3-D Turbulent Flows with Imbedded Longitudinal Vortex," *Computational Fluid Dynamics Journal*, Vol. 4, No. 4, pp. 473～488.

Kim, W. J. and Patel, V. C., 1994, "Influence of Streamwise Curvature on Longitudinal Vortices Imbedded in Turbulent Boundary Layers," *Journal of Computers Fluid*, Vol. 23, No. 5, pp. 647～673.

Kwak, D. C., Shanks, S. P. and Chakravarthy, S., 1986, "A Three-Dimensional Incompressible Navier-Stokes Flow Solver Using Primitive Variables," *AIAA Journal*, Vol. 24, No. 3, pp. 390～396.

Lee, Y. K. and Kim, H. D., 2004a, "Vortical Flows over a Delta Wing at High Angles of Attack," *KSME International Journal*, Vol. 18, No. 8, pp. 1042～1051.

Lee, Y. K. and Kim, H. D., 2004b, "Vortical Flows over a LEX-Delta Wing at High Angles of Attack," *KSME International Journal*, Vol. 18, No. 12, pp. 2273～2283.

Lowson, M. V., 1989, "Visualization Measurements of Vortex Flows," *AIAA* paper 89-0191.

Pauley, W. R. and Eaton, J. K., 1988, "The Fluid Dynamics and Heat Transfer Effects of Streamwise Vortices Embedded in a Turbulent Boundary Layer," Report No. MD-51, Department of Mechanical Engineering, Stanford University.

Phillips, W. R. C. and Graham, J. A. H., 1984, "Reynolds Stress Measurements in a Turbulent Trailing Vortex," *Journal of Fluid Mechanics*, Vol. 147, pp. 353～371.

Wendt, B. J. and Hingst, W. R., 1994, "Flow Structure in the Wake of a Wishbone Vortex Generator," *AIAA Journal*, Vol. 32, No. 11, pp. 2234～2240.

Yang, J. S. and Lee, K. B., 2000, "A Numerical Simulation of Longitudinal Vortex in Turbulent Boundary Layers," *Transaction of the KSME B*, Vol. 24, No. 6, pp. 802～813.

Zhu, J. X., Mitra, N. K. and Fiebig, M., 1993, "Effects of Longitudinal Vortex Generators on Heat Transfer and Flow Loss in Turbulent Channel Flows," *International Journal of Heat and Mass Transfer*, Vol. 36, No. 9, pp. 2239～2347.